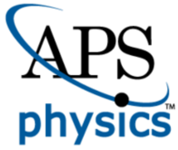

CHORUS

This is the accepted manuscript made available via CHORUS. The article has been published as:

Surface states of strained thin films of the Dirac semimetal Cd_{3}As_{2}

Manik Goyal, Honggyu Kim, Timo Schumann, Luca Galletti, Anton A. Burkov, and Susanne Stemmer

Phys. Rev. Materials **3**, 064204 — Published 18 June 2019

DOI: 10.1103/PhysRevMaterials.3.064204

The surface states of strained thin films of the Dirac semimetal Cd_3As_2

Manik Goyal[1)], Honggyu Kim[1)], Timo Schumann[1)], Luca Galletti[1)], Anton A. Burkov[2)], and Susanne Stemmer[1)*]

[1)] Materials Department, University of California, Santa Barbara, California 93106-5050, USA.

[2)] Department of Physics and Astronomy, University of Waterloo, Waterloo, Ontario, Canada N2L 3G1

[*] Corresponding author. Email: stemmer@mrl.ucsb.edu

Abstract

We report on the growth and transport properties of strained thin films of the three-dimensional Dirac semimetal Cd_3As_2. Epitaxial heterostructures, consisting of (112)-oriented Cd_3As_2 films, are grown on nearly lattice matched $(Ga_{1-x}In_x)Sb$ buffer layers on (111) GaAs substrates by molecular beam epitaxy. The epitaxial coherency strain breaks the four-fold rotational symmetry, which protects the bulk Dirac nodes in Cd_3As_2. All strained films exhibit the quantum Hall effect with most carriers residing in the two-dimensional states, irrespective of the sign of the biaxial stress. The Hall mobility monotonically increases as the biaxial stress is changed from compressive towards tensile. Furthermore, pronounced anisotropy is seen in the transport properties. The results show that the quantum Hall effect, which is quite similar to that of unstrained (112)-oriented films, is independent of the presence of bulk Dirac nodes. Its appearance is consistent with the presence of topological surface states that are a characteristic of the topological $\mathbb{Z}_2$ invariant.

I. Introduction

Cadmium arsenide (Cd_3As_2) is a three-dimensional Dirac semimetal, whose accidental degeneracies (band crossings or Dirac nodes) are protected by the four-fold rotational symmetry of its tetragonal crystal structure [1-6]. Three-dimensional Dirac semimetals also possess surface states. Depending on parameters, such as the Fermi energy and surface orientation, these surface states may form two copies of Fermi arcs, similar to those of Weyl semimetals [7, 8]. Because they are required by the $\mathbb{Z}_2$ invariant [7], surface states exist even when a band gap opens in the bulk, in analogy with three-dimensional topological insulators [8]. Experimentally, it has been shown that the transport properties of thin Cd_3As_2 films become increasingly dominated by two-dimensional states as their thickness is decreased [9, 10], eventually giving rise to a quantum Hall effect [9-12]. These two-dimensional states have been shown to exhibit characteristics of two-dimensional Dirac fermions, including a zero-energy Landau level [13]. While these observations are consistent with the presence of topological surface states, alternative interpretations of the origin of the quantum Hall effect in thin Cd_3As_2 films have also been proposed. These include subbands derived from bulk states [12] and so-called "Weyl orbits" [14], which arise from a connection between the Fermi arcs on the surface through the bulk nodes [15]. A requirement for transport through Weyl orbits is that the bulk Dirac nodes are not gapped (or disconnected from the bulk nodes [8]), even in thin slabs.

Thin film epitaxial strains break certain crystal symmetries and therefore offer opportunities to tune the electronic states and the transport properties. For example, breaking the rotational symmetry that protects the Dirac nodes is expected to open a band gap in the bulk Dirac nodes and transform the material into different kinds of insulators [16, 17]. Strain engineering requires epitaxial thin films on closely lattice matched substrates or buffer layers.

We have previously reported on the properties of epitaxial, (112)-oriented Cd_3As_2 films on (111) GaSb epitaxial buffers on (111)GaAs, which were grown by molecular beam epitaxy (MBE) [18]. These Cd_3As_2 films grew with their relaxed (bulk) lattice parameter because of the large lattice mismatch between GaSb (a = 6.096 Å) and Cd_3As_2 (a =12.6 Å – 12.7 Å and c = 25.4 – 25.5 Å; the ranges reflect the different reported values [19, 20]).

In this study, we investigate the transport properties of strained Cd_3As_2 films that are grown on $(Ga_{1-x}In_x)Sb$ alloy buffer layers. The larger lattice parameter of InSb (a = 6.479 Å) allows for alloys that are more closely lattice-matched to Cd_3As_2, as needed for strained films. Furthermore, to maintain coherently strained films, their thicknesses must be below the critical value for strain relaxation. Here, we report on the properties of films in the thickness regime in which unstrained films exhibit the quantum Hall effect [9, 10].

II. Experimental Methods

Cd_3As_2 films were grown by MBE on relaxed, epitaxial $(Ga_{1-x}In_x)Sb$ buffer layers on (111)B GaAs substrates with a miscut of 3° towards $\langle\bar{1}\bar{1}2\rangle$. The Cd_3As_2 MBE parameters have been reported elsewhere [18, 21]. The In-content of the buffer layers (x), and thus their lattice parameter, was systematically varied. All Cd_3As_2 films exhibited streaky reflections in high-energy electron diffraction (RHEED) patterns, indicating smooth surfaces, and all showed similar surface morphologies, independent of the film strain [22]. Film thicknesses were determined using x-ray reflectivity and transmission electron microscopy. X-ray diffraction (XRD) and reflectivity measurements were carried out in a Panalytical MRD PRO Materials Research Diffractometer, using Cu Kα (1.5405 Å) radiation with a triple axis Ge (220). For high-angle annular dark-field (HAADF) imaging, cross-section samples of Cd_3As_2 films were

prepared using a FEI Helios Dualbeam NanoLab 650 focused ion beam (FIB) system with the final milling voltage of 2keV Ga ions. HAADF imaging in scanning transmission electron microscopy (STEM) was carried out using a FEI Titan S/TEM (C_s = 1.2 mm) at 300 keV with a semi-convergence angle of 9.6 mrad. To improve the signal-to-noise ratio, 30 images (1024 × 1024 pixels, 1 μsec dwell time) were sequentially recorded, rigidly registered using a cross-correlation method, and then averaged. For transport measurements, Hall bar structures with dimensions of 100×100 μm^2 or 50×50 μm^2 were processed by optical lithography and Ar ion milling. The Cd_3As_2 surface was cleaned using a N_2 plasma before the measurements, which reduces carrier depletion and moves the Fermi level into the surface states, as described elsewhere [23]. The Hall resistance as a function of magnetic field (B) was linear, indicating a single dominant carrier after the N_2 plasma treatment, whereas before the treatment both *n*- and *p*-type carriers contribute, as discussed elsewhere [23]. Measurements were carried out in a Physical Property Measurement System at temperatures down to 2 K and under magnetic fields of up to 9 T.

III. Results and Discussion

Figure 1(a) shows out-of-plane XRD scans around the 111 $(Ga_{1-x}In_x)Sb$ and the 224 Cd_3As_2 reflections, respectively, for four different buffer layer compositions. The Cd_3As_2 film thickness was ~ 80 nm, to obtain a sufficient signal from the film peaks. The literature values for the lattice parameter of Cd_3As_2 vary [19, 20]; here, we show as a reference [see vertical line in Fig. 1(a)] the average position of the 224 reflection of relaxed Cd_3As_2 films on (111)GaSb buffers. In case of biaxial compressive film stress [bottom two scans in Fig. 1(a)], the shift in the 224 peak positions indicated the expected larger out-of-plane lattice parameter. Film strains

were difficult to estimate because of significant peak overlap. The film with the largest compressive in-plane strain (~ -0.4%) in Fig. 1(a) had a well-separated film peak. Cross-section HAADF-STEM showed coherent interfaces free of misfit dislocations for films under biaxial compressive stress (Fig. 2). In contrast, films that were under a (nominal) biaxial tensile stress had lattice parameters close to those of relaxed Cd_3As_2 [see top scan in Fig. 1(a)]. Transmission electron microscopy showed semicoherent interfaces [22]. The reason why tensile films showed onset of strain relaxation below the estimated critical thickness is presently not understood. Part of the reason may be the additional tensile strain from the thermal mismatch, estimated to be about 0.1% [24].

Figure 1(b) shows the electron mobilities of ~ 30-nm-thick films, determined from the low-field Hall effect, which varied systematically with film strain. The Hall mobility of tensile films was more than an order of magnitude larger than that of compressive films. The systematic change in mobility as a function of the film strain indicated that all 30-nm-thick films were strained, including those for which misfit dislocation were observed, indicating only partial relaxation of the lattice mismatch. Indeed, films grown on buffer layers with larger lattice constants than those in Fig. 1(b) showed a sharp reduction in mobility to ~ 5,000 cm^2/Vs, indicating complete strain relaxation.

Figure 3 shows representative transverse (R_{xy}) and longitudinal (R_{xx}) resistances as a function of B for ~30-nm-thick films for compressive and tensile stresses, respectively. Onset of quantized Hall plateaus in R_{xy} and pronounced quantum oscillations in R_{xx} were seen for all films, including those with strains in between those of the films in Fig. 3 (not shown). In this aspect, the films behaved very similar to relaxed Cd_3As_2 films of similar thickness, grown on (111) GaSb buffer layers [9, 10]. The carrier density determined from the quantum oscillations

was ~ 5×10^{11} cm^{-2} for all films, indicating a constant carrier concentration in the two-dimensional states. The carrier density estimated from the low-field Hall data (B < 0.5 T), ranged from 6.5×10^{11} cm^{-2} for the tensile films to 14×10^{11} cm^{-2} for the compressive films. Discrepancies between the two values occur when bulk carriers contribute to the Hall effect, via thermal excitation. Epitaxial strains can modify the band structure and they can also modify the activation energies of defects giving rise to unintentional doping [25]. Here, the films under compressive stresses, like the unstrained films [9], showed thermally activated transport behavior. The activation energies were somewhat larger than in the unstrained case, but it is unclear if these reflect intrinsic changes in the band structure or the activation energy of a defect.

The fact that the quantum Hall effect was observed for both signs of biaxial film stress indicated that neither sign of strain eliminates the two-dimensional states, i.e., they are robust against the breaking of the four-fold rotational symmetry by the biaxial film stress. The Hall plateaus were less well-resolved for compressively strained films. As the carrier densities in the two-dimensional states were similar, this indicated a greater degree of broadening of the Landau levels in compressive films, concurrent with the significantly lower Hall mobility.

The strained films had significantly lower symmetry than unstrained films, as evidenced by a pronounced in-plane anisotropy in the zero-field transport properties not seen in unstrained films. Figure 4 shows values for R_{xx} and R_{xy} measured in zero-field along different directions of a compressively strained film using Hall bar structures arranged in a circular pattern [see Fig. 4(a)]. A similar transverse voltage was observed for tensile films. Note that the appearance of a transverse voltage is not due to the Hall effect but is a sign of anisotropy. Specifically, for a second rank tensor property measured along directions that do not coincide with the principal axes [26]:

$$R_{xx} = R_a \cos^2\theta + R_b \sin^2\theta \tag{1a}$$

$$R_{xy} = -R_a \sin\theta\cos\theta + R_b \sin\theta\cos\theta, \tag{1b}$$

where R_a and R_b are the principal components of the tensor and θ describes the angle of rotation from the principal axes of the crystal system. The dashed lines in Fig. 4 are fits using Eq. (1), which described the experimental data reasonably well. In contrast, bulk Cd_3As_2 is very nearly cubic and the resistivity is thus expected to be fairly isotropic. In keeping with this expectation, relaxed films on GaSb did not develop transverse voltages under zero applied field, as confirmed by measurements on films on different substrates and with different miscuts. Strained films thus have considerably lower symmetry than unstrained films also in their transport properties.

IV. Conclusions

To briefly summarize the findings, we have shown that strained, epitaxial (112) Cd_3As_2 films can be obtained on epitaxial (111) $(Ga_{1-x}In_x)Sb$ buffer layers. All strained films showed the quantum Hall effect at high magnetic fields, indicating that transport was predominately via two-dimensional states, and thus similar to unstrained films of comparable thicknesses. This is significant, because strain in (112) oriented films breaks the 4-fold rotational symmetry and thus eliminates the bulk Dirac points. Similarly, thin films are expected to open a band gap in the bulk nodes due to confinement and/or structure inversion asymmetry [27, 28]. Tensile in-plane strains may further increase the band gaps created by confinement and breaking of the four-fold rotational symmetry [25]. The important point is that quantum Hall effect is therefore unlikely to be associated with "Weyl orbits", which depend on the presence bulk Dirac points. Along with our previous studies, the results provide further evidence that the quantum Hall effect in Cd_3As_2 films originates from the surface states themselves. Specifically, these surface states are required

by the $\mathbb{Z}_2$ invariant, as mentioned in the Introduction. They are identical to the surface states of time reversal invariant topological insulators and reside at the center of the surface Brillouin zone, independently of the bulk Dirac points [7]. The quantum Hall arises from these surface states, in analogy with expectations from topological insulators [29].

Theoretical calculations by Bednik [17] have shown that in Dirac semimetals with broken rotational symmetry, such as studied here, a second, distinct type of surface states may exist. This second kind requires the presence of mirror symmetries and results from a nontrivial mirror Chern number, which appears when the bulk Dirac points are gapped out. Based on the calculations in ref. [17], it is possible that as a function of film strain, topological phase transitions may thus occur, at which the number of surface state branches changes. Experiments that could distinguish between these different topological surface states will be a subject of future investigations.

In general, the effects of epitaxial film strains can be quite complex as they depend on the specifics of the electronic bands and their deformation potentials. To clarify these details, electronic structure calculations would be extremely useful. Such calculations would also be highly beneficial towards understanding the systematic change in mobility with strain observed here and the systematic increase of bulk-like carriers with compressive in-plane strain. While the change in mobility cannot entirely be explained with different defect densities, which should be similar in all films, changes in the electronic structure may influence both the effective band mass and the carrier scattering, both of which can contribute to the carrier mobility.

Acknowledgments

The authors thank David Kealhofer, Christopher Freeze, and Omor Shoron for useful discussions and Nikita Salunke and Jade Chongsathapornpong for assistance with the experiments. The authors gratefully acknowledge support through by a Vannevar Bush Faculty Fellowship program by the U.S. Department of Defense (grant no. N00014-16-1-2814). The collaboration between researchers at the University of California, Santa Barbara, and the University of Waterloo was performed under the auspices of the CATS Energy Research Frontier Center, which is funded by the Department of Energy, Basic Energy Sciences, under contract DE-AC02-06CH11357. The microscopy work was supported by the U.S. Department of Energy (Grant No. DEFG02-02ER45994). The work made use of the MRL Shared Experimental Facilities, which are supported by the MRSEC Program of the US National Science Foundation under Award No. DMR 1720256.

References

[1] Z. J. Wang, H. M. Weng, Q. S. Wu, X. Dai, and Z. Fang, Phys. Rev. B **88**, 125427 (2013).

[2] S. Borisenko, Q. Gibson, D. Evtushinsky, V. Zabolotnyy, B. Buchner, and R. J. Cava, Phys. Rev. Lett. **113**, 165109 (2014).

[3] Z. K. Liu, J. Jiang, B. Zhou, Z. J. Wang, Y. Zhang, H. M. Weng, D. Prabhakaran, S.-K. Mo, H. Peng, P. Dudin, T. Kim, M. Hoesch, Z. Fang, X. Dai, Z. X. Shen, D. L. Feng, Z. Hussain, and Y. L. Chen, Nat. Mater. **13**, 677 (2014).

[4] M. Neupane, S. Y. Xu, R. Sankar, N. Alidoust, G. Bian, C. Liu, I. Belopolski, T. R. Chang, H. T. Jeng, H. Lin, A. Bansil, F. Chou, and M. Z. Hasan, Nat. Comm. **5**, 3786 (2014).

[5] S. Jeon, B. B. Zhou, A. Gyenis, B. E. Feldman, I. Kimchi, A. C. Potter, Q. D. Gibson, R. J. Cava, A. Vishwanath, and A. Yazdani, Nat. Mater. **13**, 851 (2014).

[6] S. M. Young, S. Zaheer, J. C. Y. Teo, C. L. Kane, E. J. Mele, and A. M. Rappe, Phys. Rev. Lett. **108**, 140405 (2012).

[7] B.-J. Yang, and N. Nagaosa, Nat. Comm. **5**, 4898 (2014).

[8] M. Kargarian, M. Randeria, and Y. M. Lu, Proc. Natl. Acad. Sci. **113**, 8648 (2016).

[9] T. Schumann, L. Galletti, D. A. Kealhofer, H. Kim, M. Goyal, and S. Stemmer, Phys. Rev. Lett. **120**, 016801 (2018).

[10] M. Goyal, L. Galletti, S. Salmani-Rezaie, T. Schumann, D. A. Kealhofer, and S. Stemmer, APL Mater. **6**, 026105 (2018).

[11] C. Zhang, A. Narayan, S. Lu, J. Zhang, H. Zhang, Z. Ni, X. Yuan, Y. Liu, J.-H. Park, E. Zhang, W. Wang, S. Liu, L. Cheng, L. Pi, Z. Sheng, S. Sanvito, and F. Xiu, Nat. Comm. **8**, 1272 (2017).

[12] M. Uchida, Y. Nakazawa, S. Nishihaya, K. Akiba, M. Kriener, Y. Kozuka, A. Miyake, Y. Taguchi, M. Tokunaga, N. Nagaosa, Y. Tokura, and M. Kawasaki, Nat. Comm. **8**, 2274 (2017).

[13] L. Galletti, T. Schumann, O. F. Shoron, M. Goyal, D. A. Kealhofer, H. Kim, and S. Stemmer, Phys. Rev. B **97**, 115132 (2018).

[14] C. Zhang, Y. Zhang, X. Yuan, S. Lu, J. Zhang, A. Narayan, Y. Liu, H. Zhang, Z. Ni, R. Liu, E. S. Choi, A. Suslov, S. Sanvito, L. Pi, H.-Z. Lu, A. C. Potter, and F. Xiu, Nature **565**, 331 (2019).

[15] P. J. W. Moll, N. L. Nair, T. Helm, A. C. Potter, I. Kimchi, A. Vishwanath, and J. G. Analytis, Nature **535**, 266 (2016).

[16] D. Shao, J. Ruan, J. Wu, T. Chen, Z. Guo, H. Zhang, J. Sun, L. Sheng, and D. Xing, Phys. Rev. B **96**, 075112 (2017).

[17] G. Bednik, Phys. Rev. B **98**, 045140 (2018).

[18] T. Schumann, M. Goyal, H. Kim, and S. Stemmer, APL Mater. **4**, 126110 (2016).

[19] M. N. Ali, Q. Gibson, S. Jeon, B. B. Zhou, A. Yazdani, and R. J. Cava, Inorg. Chem. **53**, 4062−4067 (2014).

[20] G. A. Steigmann, and J. Goodyear, Acta Cryst. **B24**, 1062 (1968).

[21] T. Schumann, M. Goyal, D. A. Kealhofer, and S. Stemmer, Phys. Rev. B **95**, 241113 (2017).

[22] See Supplemental Material [link to be inserted by publisher] for atomic force microscopy images of the film surfaces and cross-section HAADF-STEM images of a film on a tensile buffer.

[23] L. Galletti, T. Schumann, T. E. Mates, and S. Stemmer, Phys. Rev. Mater. **2**, 124202 (2018).

[24] A. Pietrasz, and K. Lukaszew, Phys. Status Solidi A **18**, 723 (1973).

[25] A. V. Germanenko, and G. M. Minkov, Phys. Stat. Sol. B **184**, 9 (1994).

[26] J. F. Nye, *Physical Properties of Crystals* (Clarendon Press, Oxford, 1985).

[27] A. Narayan, D. Di Sante, S. Picozzi, and S. Sanvito, Phys. Rev. Lett. **113**, 256403 (2014).

[28] S. B. Zhang, H. Z. Lu, and S. Q. Shen, Sci. Rep. **5**, 13277 (2015).

[29] L. Brey, and H. A. Fertig, Phys. Rev. B **89**, 085305 (2014).

Figure Captions

Figure 1: (a) θ-2θ XRD scans around the out-of-plane 224 reflection of a 80 nm Cd_3As_2 film and that of the 111 $(Ga_{1-x}In_x)Sb$ buffer layer reflections, respectively, for different buffer layer compositions *x*. The In compositions of the buffer layers (top to bottom) are x = 0.75, 0.69, 0.64, and 0.60, respectively. The dashed line indicates the average position of the 224 peak of relaxed Cd_3As_2 films on GaSb buffers. Film reflections to the left of the buffer layer reflection are consistent with compressive in-plane strains. (b) Hall mobilities of Cd_3As_2 films grown on $(Ga_{1-x}In_x)Sb$ buffer layers with different compositions, measured along the $[\bar{1}10]$ direction of the buffer layer at 2 K. The horizontal axis shows the buffer layer lattice parameter and the dashed line indicates the average lattice parameter of relaxed Cd_3As_2 films on GaSb.

Figure 2: (a) High-resolution, cross-section HAADF-STEM image of a compressively strained Cd_3As_2 film on a $(Ga_{0.4}In_{0.6})Sb$ buffer layer, showing an abrupt interface with no visible defects at the interface. (b) Schematic of the structure of Cd_3As_2 (space group $I4_1/acd$ [19]) projected along $[1\bar{1}0]$. The image intensities in (a) are consistent with this structure, especially the arrangements of the columns containing Cd vacancies (light purple dots), which have lower intensities. (c) Intensity profiles obtained from the green and blue shaded boxes in (a) further confirm the presence of ordered Cd vacancies in the crystal structure (see red arrows).

Figure 3: Hall resistance (top row) and magnetoresistances (bottom row) measured at 2 K for 30 nm thick films under different biaxial stresses. Data shown in (a,c) is from a (partially) relaxed film grown under tensile stress (x = 0.75), data in (b, d) is from a film under compress

stress on a buffer with $x = 0.64$. The in-plane compressive strain is about -0.2%. Films with up to -0.3% strain showed similar behavior. The film thickness were ~ 30 nm.

Figure 4: (a) Schematic of the Hall bar structure used to measure longitudinal and transverse resistances along different directions of a compressively strained film. The contact pads are not shown for clarity. The crystallographic directions indicated are those of the substrate and the angles are defined in (a). (b, c) Measured values for R_{xx} and R_{xy} as a function of the direction. The dashed lines are fits to Eq. (1).

(a)

Cd_3As_2

Cd_3As_2

Intensity (arb. units)

24.0 24.1 24.2 24.3 24.4 24.5

2θ (°)

(b)

Hall mobility ($m^2V^{-1}s^{-1}$)

0.0 0.2 0.4 0.6 0.8 1.0 1.2 1.4

6.32 6.34 6.36 6.38

a_{buffer} (Å)

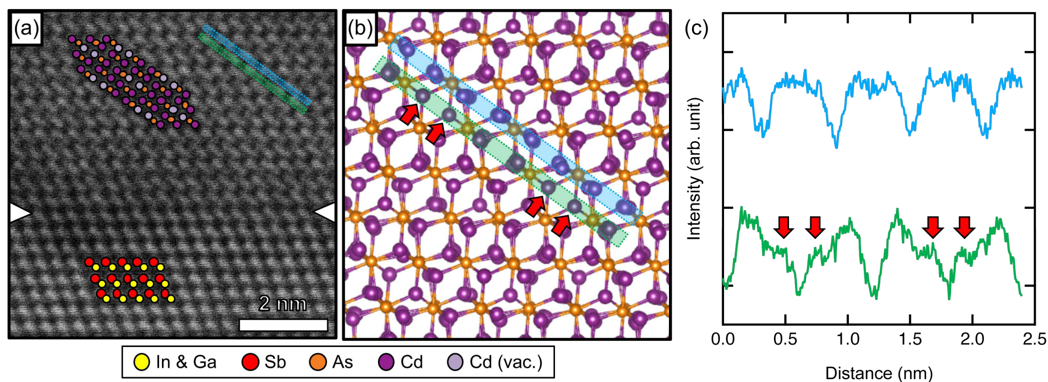

(a)
2 nm
(b)
(c)
Intensity (arb. unit)
0.0
0.5
1.0
1.5
2.0
2.5
Distance (nm)
In & Ga
Sb
As
Cd
Cd (vac.)

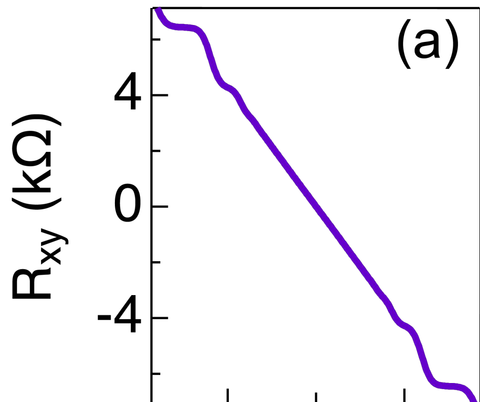
(a)
R_{xy} (kΩ)
4
0
-4

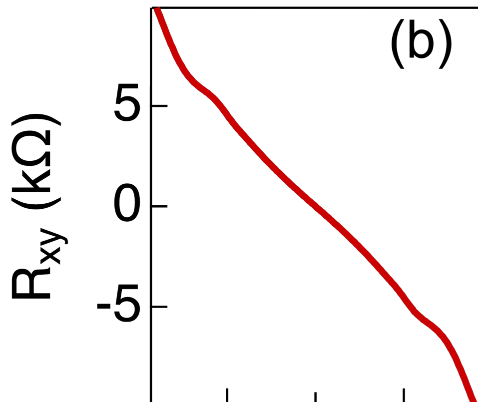
(b)
R_{xy} (kΩ)
5
0
-5

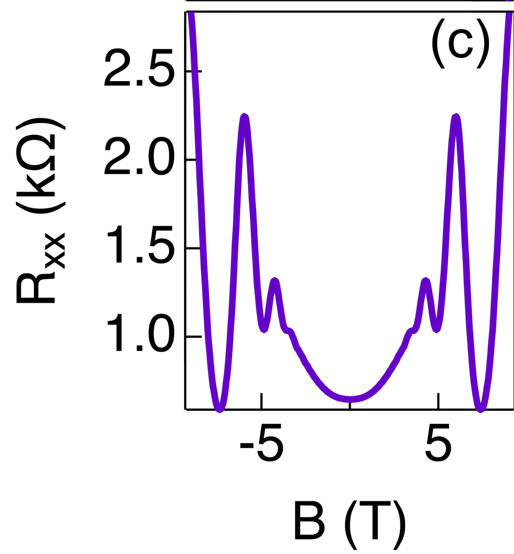
(c)
R_{xx} (kΩ)
2.5
2.0
1.5
1.0
-5
5
B (T)

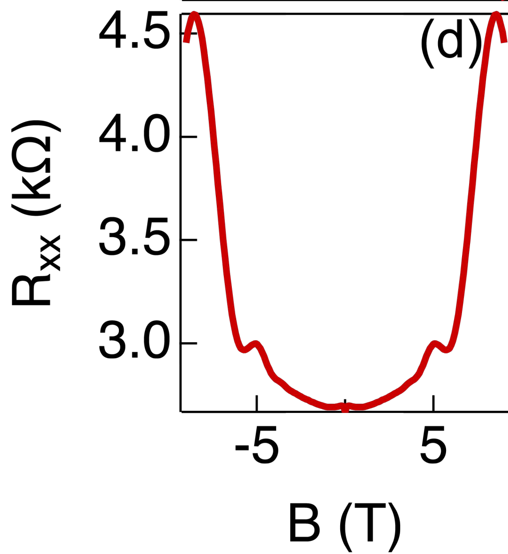
(d)
R_{xx} (kΩ)
4.5
4.0
3.5
3.0
-5
5
B (T)

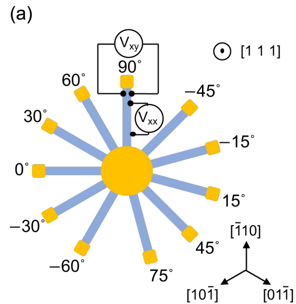
(a)
V_xy
90°
60°
−45°
V_xx
30°
−15°
0°
15°
−30°
45°
−60°
75°
[1 1 1]
[1̄10]
[101̄]
[011̄]

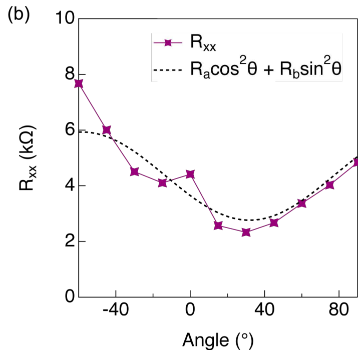
(b)
R_xx
R_a cos²θ + R_b sin²θ
R_xx (kΩ)
Angle (°)

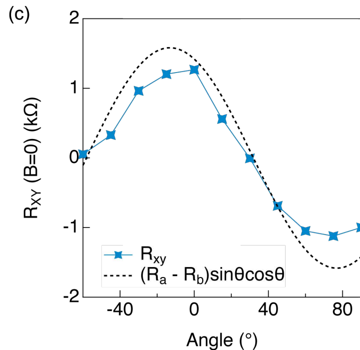
(c)
R_xy
(R_a - R_b)sinθcosθ
R_XY (B=0) (kΩ)
Angle (°)